

Award Accounts

The Chemical Society of Japan Award for Young Chemists for 2006

Development of Novel Near-Field Microspectroscopy and Imaging of Local Excitations and Wave Functions of Nanomaterials

Kohei Imura* and Hiromi Okamoto

Institute for Molecular Science and the Graduate University for Advanced Studies, Myodaiji, Okazaki 444-8585

Received January 9, 2008; E-mail: imura@ims.ac.jp

We have developed novel methods of near-field microspectroscopy by combining near-field optical microscopy with linear and non-linear optical techniques. The developed near-field microscope achieves high spatial resolution and high time resolution, and is applied to studies of local excitations and wave functions of single noble metal nanoparticles. We demonstrate that the plasmon wave functions and the optical fields in the vicinity of nanoparticles are visualized by the near-field methods. Based on these results, we clearly show that localized electromagnetic field enhancement in the vicinity of nanoparticles is one of the most important factors in surface-enhanced spectroscopies. We also extended the methods to ultrafast optical measurements, and show space-resolved ultrafast transient response of single gold nanorods. The characteristic spatio-temporal features observed in the nanorods are revealed to be arising from the changes of the plasmon-mode wave functions upon elevation of photo-induced electronic temperature of the nanorod.

1. Introduction

Visualization of objects with a nanometer spatial resolution is enormously important in a wide range of science and technology. Investigation of electronic structures and their dynamic properties at a nanometer spatial scale are essential especially in nanomaterials science. In order to attain direct access to the fundamental nature of these characteristic properties of nanomaterials, spectroscopic tools with high spatial- and time-resolutions are required.[1] Modern optical techniques have achieved very high spectral- and time-resolution. However, spatial resolution of the optical measurement is limited to about half of the wavelength as far as the method is based on the conventional optical microscope, because of the diffraction limit of light.[2,3]

For the purpose of improving spatial resolution beyond the conventional optical microscope, the scanning electron microscope (SEM) and the transmission electron microscope (TEM) were invented several decades ago, and in these few decades, scanning probe microscopies (SPMs), such as the scanning tunneling microscope (STM) and the atomic force microscope (AFM), have also been developed. These microscopes can map the topography of an object with an ultimate spatial resolution close to or even beyond the atomic scale. However, at the expense of spatial resolution, optical contrasts in nanomaterials are not obtained in these methods.

In the late 1980s and early 1990s, near-field optical methods were proposed and demonstrated as a new optical technique to improve spatial resolution.[4,5] Near-field methods are based on the property of evanescent waves (localized photons), and spatial resolution is not diffraction-limited. By combining the principle of the near-field method with the SPM technique, a scanning near-field optical microscope (SNOM) has been developed,[6–8] and it allows us to obtain spectroscopic information with nanometer spatial resolution. An advantage of the near-field method is not only its high spatial resolution, but also its potential compatibility with various advanced spectroscopic techniques developed in the field of laser spectroscopy.[9–11]

Among nanomaterials, noble metal nanoparticles have attracted significant attention for their ability to manipulate optical properties at the nanometer scale,[12] which originate from the nature of localized surface plasmon (LSP) resonances.[13,14] Surface plasmons (SPs) are the collective oscillation of conduction electrons excited in the presence of an electromagnetic field.[15] In the case of noble metal particles, LSP resonance is excited by photons in the spectral region from visible to near-infrared. Resonance wavelength of LSP is dependent upon the size, shape, and local environment of the nanoparticle. This is the origin of the unique reddish colors of gold colloids, which have been employed in the staining of glass windows and ceramic pottery since ancient times.

Recently, many studies of noble metal particles have focused on electromagnetic field enhancement in the vicinity of the particles.[16,17] The enhancement originates from a nanometric electromagnetic field confinement by LSP resonance. The field enhancement sometimes reaches a few orders of magnitude, when the LSP is resonantly excited. The enhancement allows us a variety of intriguing applications, such as photo-catalysis, ultrasensitive chemical/biological sensors,

Published on the web June 11, 2008; doi:10.1246/bcsj.81.659

recording media, and nano-optical devices.[18–21]

Notable aspects of the electromagnetic field due to the LSP are not only the magnitude of enhancement but also the spatial characteristics. LSP confines the electromagnetic/photon field into nanometric space, and thus the spatial scales of the photon field can be comparable with those of molecules. Under such conditions, the interaction of photons with molecules is no longer describable by the long-wavelength limit (dipole approximation), but needs a full wave electromagnetic formalism.[22] The optical localization enables dipole-forbidden transitions to be optically active.[23] Hence, the LSP can provide a new framework for photoexcitation of electronic and vibrational states, and may have significant effect on photochemical reactions.

In order to understand functions of plasmon-based nanomaterials, and to utilize them for novel photochemical processes and future nano-optical devices, static and dynamic aspects of plasmon excitation need to be elucidated. It is of special importance to reveal spatial features of plasmon excitations and wave functions at the nanometer scale. Such features are usually smaller than the diffraction limit of light, thus conventional optical microscopy is basically not applicable for this purpose.

We have developed some experimental methods of static and dynamic near-field microspectroscopy,[24,25] and the methods have been applied to reveal static and dynamic characteristics of plasmon excitations.[26,27] We have succeeded in visualizing spatial features of optical fields and plasmon wave functions in noble metal nanoparticles by using linear and non-linear near-field spectroscopic imaging techniques.[28,29] We have also extended the technique to visualize spatio-temporal behaviors of plasmon wave functions in single gold nanoparticles after photoexcitation.[27]

In this article, we review the development of near-field methods and application of them to optical-field and wave function imaging for gold nanoparticles and assemblies. The paper is organized as follows. In Sections **2** and **3**, we describe basic methods of synthesis and optical properties of gold nanoparticles. In Section **4**, we present an outline of development of near-field methods, and in Section **5**, we give a general theoretical discussion on the origin of near-field optical images. In Sections **6** to **9**, we present near-field optical studies of gold nanoparticles and assemblies: in Sections **6** and **7**, we focus on visualization of plasmon wave functions and optical fields in the vicinity of nanoparticles by using linear and non-linear near-field optical methods; in Section **8**, we discuss the mechanism of surface-enhanced spectroscopy based on near-field measurements of gold nanoparticle assemblies; in Section **9**, we present ultrafast transient imaging of single gold nanoparticles and discuss the origin of the characteristic transient images of the nanoparticles. Finally, we provide concluding remarks in Section **10**.

2. Preparations of Gold Nanoparticles

Rapid advance of nanostructure fabrication techniques such as electron-beam lithography,[30] ion-beam milling,[31] and wet-chemical synthesis[32] allows us to prepare well size- and shape-controlled nanostructures. Wet-chemical methods have an advantage against other methods in view of mass and inexpensive production of the nanoparticles that facilitates the use of the unique properties for a variety of research fields. Several groups have developed synthesis routes to prepare relatively mono-dispersed spherical and rod-shaped nanoparticles.[33–37] For other shapes of nanoparticles, however, wet-chemical methods in general suffer from low yield and/or a broad size and shape distribution.

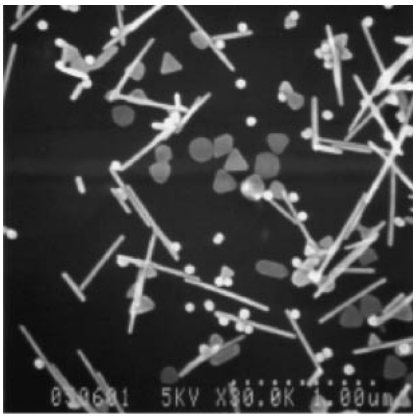

Figure 1. Scanning electron micrograph of synthesized gold nanoparticles.

2.1 Preparation of Gold Spherical Nanoparticles. Gold nanoparticles are prepared by reducing a $H[AuCl_4]$ solution with sodium citrate while boiling for several tens of minutes,[33] and spherical nanoparticles (mean diameter 20 nm and standard deviation of ca. 10%) are obtained as a colloidal water solution. In a similar way, nanoparticles with a diameter of 1 to several hundred nm can be synthesized.

2.2 Preparation of Rod-Shaped (Nanorod) and Plate-Shaped (Nanoplate) Gold Nanoparticles. Murphy and coworkers have developed synthetic protocols for the synthesis of gold nanorods and nanoplates (seed-mediated growth methods).[34,38,39] In this method, small spherical gold nanoparticles (4-nm diameter) are first prepared as seeds in water solution. This solution is then added to growth solutions which contain hexadecyltrimethylammonium bromide (CTAB) to create micelles in water. Upon addition of the seeds, a growth reaction takes place on the seed surface to produce gold nanorods and nanoplates. In the growth process, CTAB play key roles for the anisotropic growth of the nanoparticles. By tuning the reaction conditions, gold nanorods (diameter 15–40 nm, length 40–600 nm) and nanoplates (thickness 15–20 nm, base length 100–400 nm) are synthesized. This method yields crystalline gold nanoparticles. Figure 1 shows a SEM image of the synthesized nanoparticles.

3. Optical Properties of Noble Metal Nanoparticles

Optical properties of noble metal particles are strikingly different from those of their bulk or thin films.[40] Figure 2a shows the extinction spectrum of spherical gold nanoparticles suspended in water. Spherical nanoparticles (diameters $\leq$ 40 nm) exhibit a strong absorption (extinction) band near 520 nm due to dipolar plasmon resonance, resulting in a deep red color of the colloidal solution. By contrast, the film absorbs photons of the visible to near-infrared region, due to excitations of free electrons. A very large cross-section of light scat-

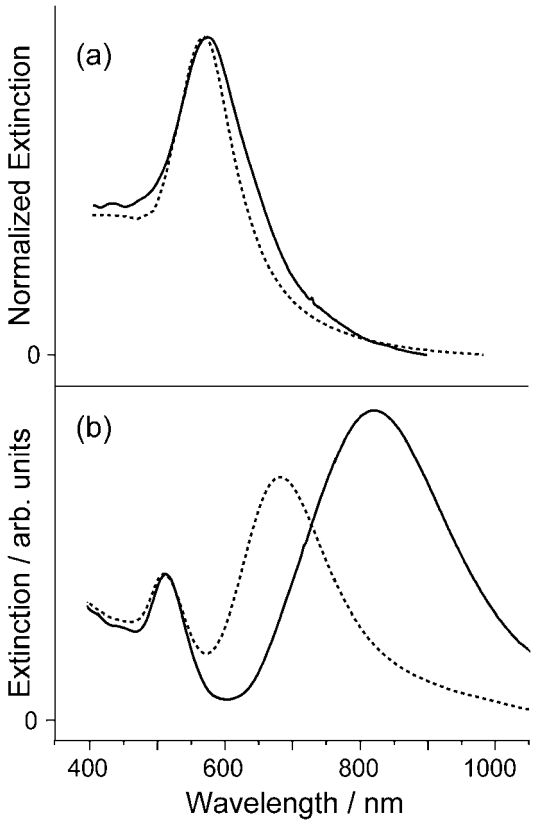

Figure 2. (a) Extinction spectrum of colloidal solution of spherical gold nanoparticles (diameter 100 nm). Solid curve: observation. Dashed curve: simulation based on the Mie theory. (b) Extinction spectra of colloidal solution of gold nanorods. Solid curve: high aspect ratio rods. Dashed curve: low aspect ratio rods.

tering is also a unique optical feature of the particles. The extinction spectrum of the colloidal solution is composed of contributions of scattering and that of optical absorption, and their spectral profiles are different from each other. For this reason, the color appearance of the colloidal solution is dependent on the view configuration. For example, a colloidal solution of gold spheres (diameter 100 nm) shows a brownish color when viewed in transmission, while appearing blue-purple in reflection. Observed color alterations are related to absorption and scattering properties of the nanoparticles.

Far-field optical properties of gold nanoparticles of other shapes have also been reported recently.[41–43] Figure 2b shows extinction spectra of gold nanorods suspended in water. Gold nanorods exhibit two bands. Based on optical polarization measurements, the band near 520 nm is assigned to a transverse LSP resonance, which is polarized across the long axis of the nanorod, and the other one appearing in a longer wavelength region is assigned to a longitudinal LSP mode, which is polarized parallel to the long axis. The longitudinal LSP resonance shifts to a longer wavelength (red shift) with increase of the aspect ratio (length/diameter) of the nanorod.

Optical properties of noble metal nanoparticles can be theoretically treated by solving Maxwell equations for scattering of electromagnetic waves. For spherical nanoparticles, Mie theory provides rigorous solutions for light scattering and absorption.[44] For other shapes, however, Mie theory is not applicable.[45] We need to solve Maxwell equations numerically by taking boundary conditions of electromagnetic field near the particle into consideration, whereas it is computationally demanding. The applicability of direct numerical simulation to practical phenomena is severely restricted. Consequently, optical properties of nanoparticles have been theoretically elucidated only for limited shapes.

It should be noted here that optical features obtained in the far-field measurements of colloidal solutions are ensemble-averaged over a number of particles with different size and shape, since it is hardly possible to prepare mono-dispersed nanoparticles. The spectral bands are therefore inhomogeneously broadened. The ensemble measurements obscure precise correlation between optical properties and nanometric structure of the particles. For deeper understanding of the optical properties of nanoparticles, single-particle spectroscopy using a SNOM provides valuable methodology.

4. Scanning Near-Field Optical Microscope (SNOM)

In 1928, Synge proposed the use of a non-radiative subwavelength light source (optical near-field) to achieve high spatial resolution beyond the diffraction limit of light.[46] He suggested to illuminate a sample through a subwavelength aperture fabricated in an opaque metal screen, and to scan the sample surface at a nanometer distance while recording the optical signal. His idea contained all the essential elements of modern SNOM. However, to realize Synge's idea, several technical hurdles (such as the fabrication of the small aperture, distance regulation in a nanometric scale, and so on) had to be cleared.

From the late 1980s to the early 1990s, technologies to overcome those difficulties were developed, and fundamental and practical SNOM measurements were established.[4–7] Since its implementation, various near-field methods were proposed and demonstrated.[8] Among them, aperture-type and scattering-type near-field optical microscopes have been widely employed. Apertured type SNOM uses a subwavelength optical aperture at the apex of a sharpened optical fiber coated with a metal.[47] Light emerging from the aperture is used to illuminate the sample. In a scattering-type near-field microscope, a sharpened metal probe is used and the local electromagnetic field enhancement at the tip by an external illumination is exploited.[13] The resolution of the aperture and the scattering SNOM is limited, respectively, by the diameter of the aperture and by the radius of curvature of the probe. Both methods can overcome the diffraction limit, and resolution of 50 nm on a routine basis is achievable and potentially as small as 10 nm.[48–50]

We have developed a novel apparatus for near-field spectroscopic techniques, by combining an apertured SNOM with various laser spectroscopic techniques. The apparatus is capable of conventional near-field linear spectroscopic measurements, as well as advanced non-linear/time-resolved methods that we have developed in this study. In time-resolved measurements, we have achieved a 50-nm spatial- and a 100-fs time-resolution simultaneously. This capability opens a new way to visualize physical properties of nanomaterials.

4.1 The Basic SNOM Setup. Figure 3 shows an experimental setup, which consists of light sources, an apertured

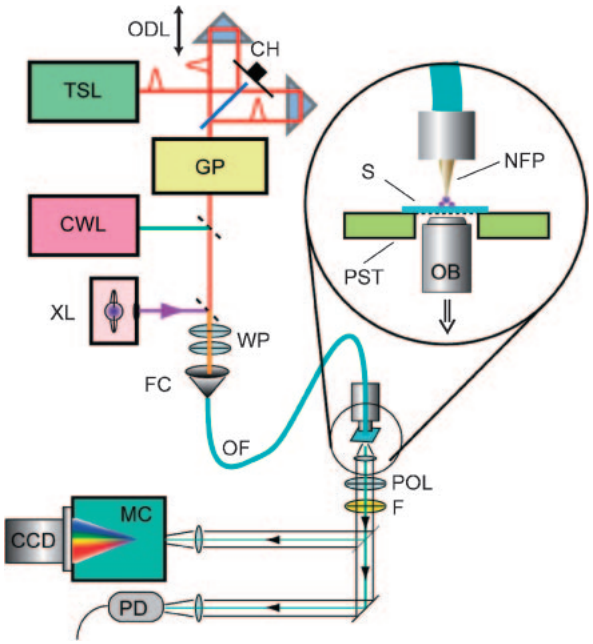

Figure 3. Schematic illustration of the near-field microscope developed. TSL: mode-locked Ti:sapphire laser, ODL: optical delay line, CH: mechanical chopper, GP: grating pair, CWL: continuous wave laser, XL: Xe discharge lamp, WP: wave plates, FC: fiber coupler, OF: optical fiber, NFP: apertured near-field probe, S: sample substrate, PST: piezo driven *xyz* stage, OB: objective lens, POL: polarizer, F: optical filter(s), PD: photodiode, MC: monochromator, CCD: charge-coupled device detector.

SNOM, and detection systems. An apertured near-field optical fiber probe is fabricated by etching a single-mode optical fiber followed by coating with a metal layer and then opening an aperture at the tip. Diameter of the aperture can be determined by a SEM observation of the probe tip itself or by a near-field fluorescence excitation image measurement of single molecules using the probe. Typical diameter of the aperture is around 50–100 nm. The optical near-field is created at the probe tip by introducing an output of a light source into the other end of the optical fiber using a fiber coupler. The sample is illuminated through the aperture of the near-field probe, and is raster-scanned beneath the near-field probe by a closed-loop piezoelectric driven stage. The use of a closed-loop stage enables reproducible and stable positioning and is essential especially when a long accumulation is required. The distance between the near-field tip and the sample surface is regulated at about a few nanometers, by using a shear-force feedback method.[7] The optical and topography images are acquired simultaneously by recording the optical and the height signals as a function of the sample position relative to the probe tip. The apparatus is operated under ambient conditions.

The light source used for the transmission spectral measurements is a Xe discharge lamp. Continuous wave (CW) lasers (λ = 532, 633, and 785 nm) are used for Raman and luminescence measurements. The samples are illuminated by radiation from these light sources through an apertured probe, and the scattered or transmitted photons are collected by an objective and detected by a polychromator equipped with a CCD. The spectra are recorded at every spatial point of the raster-scanned area.

4.2 Non-Linear Optical Measurements in SNOM. Non-linear optical methods have several advantages over linear methods. For example, non-linear methods are capable of achieving high spatial resolution and high signal-to-noise ratio, and also providing valuable spectroscopic information of atoms, molecules, and materials, that are not accessible by linear methods. Here, to perform the non-linear near-field optical measurements, we combined the SNOM apparatus described above with ultrashort light pulses from a mode-locked Ti:sapphire laser (λ = 780–920 nm, <100 fs, 80 MHz). A serious problem on the use of ultrashort pulses for an optical-fiber-based system is the group velocity dispersion (GVD) arising from the fiber (ca. 1-m long), which broadens the pulse width to several picoseconds at the near-field tip. In order to avoid the pulse broadening, the GVD arising from the fiber is pre-compensated by a grating pair before the optical pulses couples into the fiber.[25,51] In this way, initial pulse width of the laser source is recovered at the near-field tip. The short pulse width is crucial for effective excitation of the non-linear phenomena. As an example of non-linear measurements, we describe in Sections **7** and **8** optical-field imaging of gold nanoparticles and their assemblies by using near-field two-photon-excited photoluminescence (PL) technique.

Femtosecond pump–probe time-resolved near-field measurements can be performed on the setup described above with a minor modification. We have adopted equal pulse correlation to get high time resolution. In the equal pulse correlation method,[52] the pump pulse induces temporal absorption change of the sample, and the probe pulse detects the change of transmission intensity. Dynamic information at each spatial position of the sample is obtained by monitoring transmission change as a function of pump–probe delay time. For the equal pulse pump–probe measurements, output from the Ti:sapphire laser is split into two beams and both beams are mechanically chopped at different frequencies. The two optical beams are collinearly coupled to the near-field probe after pre-compensation of GVD. The GVD pre-compensation is again important to achieve high time resolution. The pump–probe signal (transient transmission change induced by the pump pulse) is detected by lock-in-detection at the difference of the chopping frequencies of the pump and probe beams. Imaging of the sample by the transient transmission intensity is also possible by scanning a sample while detecting the transient signal at a given pump–probe delay time.

5. Optical Contrast in SNOM Image

In SNOM, the principle of image formation is quite different from that of the conventional far-field optical microscope. The image formation mechanism in SNOM is thought to have an analogy with that of STM. In STM, tunneling current between the probe tip and the sample is proportional to the local density of states (LDOS) of electrons of the sample at the tip position.[53] A image of STM maps the LDOS of electrons at an energy E at a position $\vec{r}$, $\rho(\vec{r}, E)$.[54] In SNOM, "photon tunneling" between a SNOM tip and a sample plays a key role. The optical signal intensity is considered to be proportional to a photonic (or electromagnetic) LDOS. According to this idea,

a SNOM image maps the photonic LDOS $\rho(\vec{r},\omega)$ at an optical angular frequency ω at position $\vec{r}$.

The photonic LDOS is defined, using the complete set of orthonormal electromagnetic eigenfunctions $\phi_n(\vec{r})$ of the system studied, as[55]

$$\rho(\vec{r},\omega) = \sum_n \delta(\omega - \omega_n)\phi_n(\vec{r})\phi_n{}^*(\vec{r}), \quad (1)$$

where ω_n represents the n-th electromagnetic eigen frequency. Hence, LDOS at an optical frequency near the resonance with the eigen state n (i.e., $\omega \approx \omega_n$) is approximately equivalent to the square modulus of the wave function associated to the n-th photonic eigen mode. Therefore, imaging of the LDOS by a SNOM leads to a direct optical observation of the spatial distribution of the photonic wave functions.[56]

In this review, we show some calculated photonic LDOS around a sample using a Green dyadic method,[57,58] to analyze observed near-field optical images. LDOS is extracted from the Green dyadics using the relation[55,57]

$$\rho(\vec{r},\omega) = -\frac{1}{\pi}\mathrm{Tr}[\mathrm{Im}\{\overleftrightarrow{G}(\vec{r},\vec{r},\omega)\}], \quad (2)$$

where Tr and Im stand for trace and imaginary part of $\overleftrightarrow{G}(\vec{r},\vec{r},\omega)$, respectively. The Green dyadic $\overleftrightarrow{G}(\vec{r},\vec{r}',\omega)$ of the entire scattering system is numerically obtained by solving the self-consistent discretized Dyson's equation, starting from the analytically known Green dyadic of the homogeneous medium.[59] The formalism allows us to deal with an arbitrary shape of nanoparticle.

6. Near-Field Transmission Measurements

The near-field version of transmission (absorption) spectroscopy has been little utilized mainly because of the limitation of spectral range available in the near-field. The use of a tunable laser is not straightforward due to the presence of fiber coupler which suffers from chromatic aberration, and also due to the limited tunable range of the laser sources. Topographic artifacts (a kind of ghost optical image of the sample topography arising from the throughput changes of the whole optical system, due to the z-motion of the near-field probe) sometimes also interfere with obtaining genuine optical information from near-field transmission measurements.[60] For the purpose of fully utilizing near-field transmission imaging and spectroscopy, we use a Xe discharge lamp as a spectrally broad light source. At the same time, we exploit a pseudo constant height operation mode[24,61,62] to minimize the topographic artifact, when it is applicable. Under this operation mode, the probe moves at approximately constant height from the substrate in the neighboring area of the nanoparticle observed. The method allows us to obtain a genuine near-field optical signal over a wide spectral range and makes it possible to get a deeper understanding of the optical properties of nanomaterials.

In near-field transmission-spectral measurement, transmission spectra are measured at each point on the sample surface, typically 10-nm steps across the scan areas. The transmission is defined as $-(I - I_0)/I_0$, where $I(x)$ and I_0 denote the measured intensities at the sample material and at the substrate, respectively.

6.1 Single Spherical Gold Nanoparticles.[24] Figure 4a shows a near-field transmission spectrum of a single spherical gold nanoparticle (diameter 100 nm). Positive and negative values of the vertical scale correspond to reduction and enhancement of transmission intensity with respect to that observed at the substrate, respectively. The near-field transmission spectrum of a gold spherical nanoparticle exhibits enhanced transmission near 720 nm. The enhancement is not due to emission from the particle, but due to a phenomenon characteristic of the near-field measurement. In the apertured near-field microscope, evanescent waves (optical near-field) are localized in the close vicinity of the aperture and do not propagate into the far-field. Once the evanescent wave interacts with materials such as a gold nanoparticle, the wave is converted into propagating wave, which is radiative into the far-field. The enhanced transmission observed in Figure 4a is attributed to the conversion of the evanescent wave into a propagating wave. In the process of interaction between the evanescent wave and the particle, photon energy is partly damped in the particle (corresponding to absorption of light). The reduction of transmission observed near 520 nm is attributed to the absorption and scattering due to the dipolar plasmon resonance of the particle. From the near-field measurements of single spherical particles with different sizes, the dipolar plasmon resonance wavelength of the spherical nanoparticle is found to shift toward a longer wavelength from 520 to 580 nm with increasing the diameter from 10 to 100 nm. This finding is in very good agreement with the prediction by Mie theory.[12,44] The developed near-field transmission microscope has the capability to obtain an optical spectrum of a single

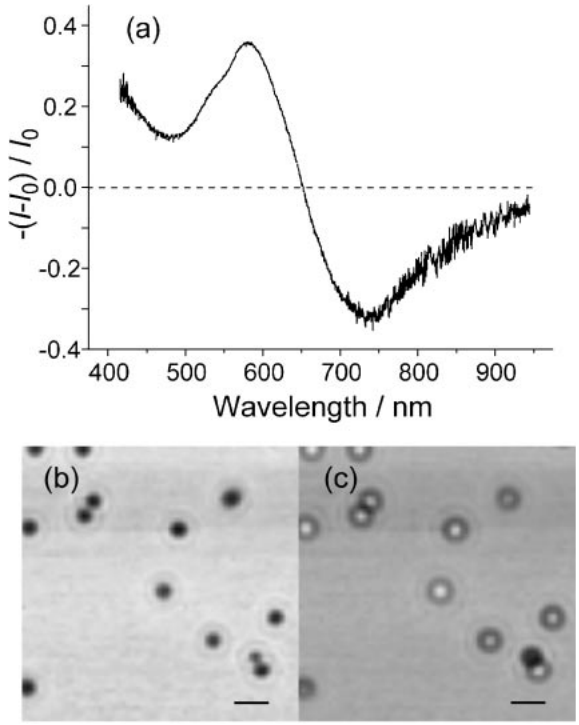

Figure 4. (a) Near-field transmission spectrum of a single spherical gold nanoparticle (diameter 100 nm). (b,c) Near-field transmission images of spherical gold nanoparticles (diameter 100 nm) taken at ≈520 and ≈720 nm, respectively. Scale bars: 1 μm (Reproduced with permission from Ref. 24. Copyright 2004, Elsevier B. V.).

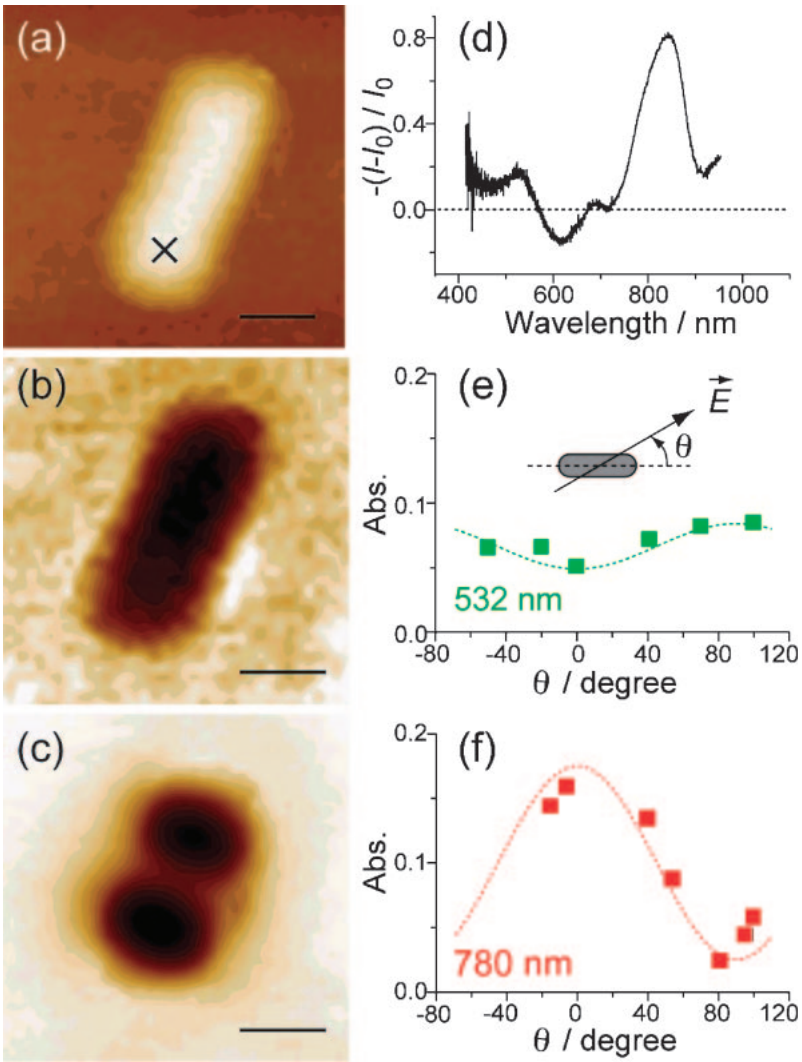

Figure 5. (a) Topography of a single gold nanorod (diameter 30 nm, length 180 nm). (b,c) Near-field transmission images observed at 520 and 780 nm, respectively. Scale bars: 100 nm. (d) Near-field transmission spectrum measured at point × in (a). (e,f) Polarization dependences of absorption bands at 532 and 780 nm at the point specified in (a) (Reproduced with permission from Ref. 27. Copyright 2004, American Chemical Society).

spherical gold nanoparticle with a diameter down to several nm.

6.2 Single Gold Nanorods. Figure 5a shows a shear-force topographic image of a single gold nanorod taken by the SNOM. The image of the nanoparticle is broadened because of the finite size (radius of curvature) of the near-field tip. By considering the broadening by the tip, the nanorod dimension (diameter × length) is estimated to be 30 nm × 180 nm (aspect ratio ≈6). Simultaneous topographic measurement by near-field microscopy is advantageous to investigate optical features of a specific point on a nanoparticle. Figure 5d shows a transmission spectrum at a crossed point (×) on the nanorod. The spectrum exhibits a few extinction bands. Polarization dependences of the bands at 520 nm (A) and 850 nm (B) show tendencies distinct from each other, as shown in Figures 5e and 5f, respectively. Band A is effectively excited when the light is polarized perpendicular to the long axis of the nanorod. On the other hand, band B is excited by the polarization parallel to the long axis of the nanorod. Dotted curves in Figures 5e and 5f indicate polarization angle dependences calculated for a perfect dipole model. Based on the polarization dependences, the bands A and B are assigned to a transverse and a longitudinal LSP resonance, respectively. It should be stressed that single-particle observation using near-field microscopy has made possible such direct assignments of optical transitions in anisotropic nanostructures.

Figures 5b and 5c show near-field transmission images (unpolarized) observed at wavelengths resonant with the two plasmon bands. Dark regions indicate reduction of the transmitted light. The transmission image at 520 nm (resonant with the transverse LSP resonance) shows a uniform reduction of transmission intensity along the long axis of the nanorod. By contrast, the transmission image taken at 780 nm (resonant with the longitudinal LSP) shows a characteristic spatially oscillatory pattern along the long axis of the nanorod. The near-field transmission at a given position of the sample reflects the optical transition probability, which is proportional to the square modulus of the LSP wave function (or the photonic LDOS as

mentioned in Section **5**) resonant with the observed wavelength. Hence, the images in Figures 5b and 5c correspond to squared amplitude mapping of the wave functions for the transverse and the longitudinal LSPs, respectively. The longitudinal-plasmon image in Figure 5c with a spatially oscillating structure is assigned to a LSP mode having a node at the center ($m_L = 2$, next to the dipolar mode). Here, the note m_L represents the mode index of longitudinal LSP, corresponding to (number of nodes) + 1. In a similar way, a small peak observed near 680 nm in the transmission spectrum (Figure 5d) is assigned to the $m_L = 3$ mode. The dipolar longitudinal mode ($m_L = 1$, usually observed most strongly in far-field measurements) is expected to appear far beyond the observed spectral range. In Figure 5b, on the other hand, the transverse-plasmon image appears rather uniform. This is because the images of the wave functions of various transverse modes are spatially overlapped with each other, due to the weak dispersion of the transverse modes.

Figure 6a shows a near-field transmission spectrum of a single gold nanorod with a higher aspect ratio (≈26). In contrast with Figure 5d, many resonance peaks appear in the spectrum. A relatively broad absorption band centered at ca. 520 nm is found and is again assigned to the transverse mode. Other resonance peaks observed at longer wavelengths can be attributed to the longitudinal LSP resonances, judging from the polarization characteristics observed.

To associate the observed spectral characteristics with photonic density-of-states (DOS), electromagnetic calculations were performed. Figure 6b shows a calculated DOS spectrum for a single gold nanorod with a diameter of 20 nm and a length of 520 nm, as a function of optical wavelength. Several resonances are clearly seen in accordance with the observed spectrum shown in Figure 6a. The observed peak positions are well reproduced by the calculation. The agreements indicate that the observed near-field transmission spectrum strongly reflects the photonic DOS feature of the gold nanorod.

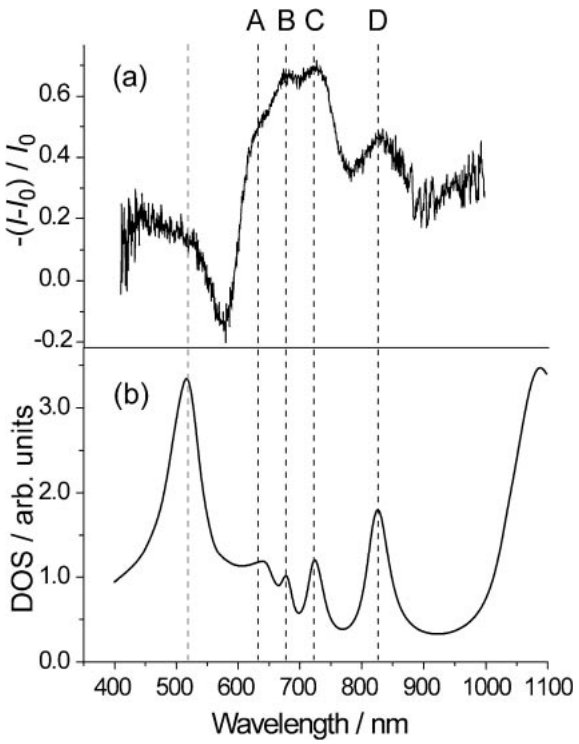

Figure 6. (a) Near-field transmission spectrum of a single gold nanorod (diameter 20 nm, length 510 nm) observed at the end-edge. (b) Calculated density-of-states spectrum of a single gold nanorod (diameter 20 nm, length 520 nm). Dotted lines are guides to the eyes for the resonance wavelengths of plasmon modes.

Figures 7a–7d show near-field transmission images of the same nanorod observed at plasmon resonance wavelengths indicated in Figure 6a (A–D). The dark part indicates the region of reduction (extinction) of the transmitted light. Each image again shows a characteristic spatial oscillating pattern, indicating that the transition probability oscillates spatially along the long axis of the nanorod. These features are assigned to spatial characteristics of the longitudinal LSP modes with higher m_L excited in the nanorods. The number of oscillations (local maxima) decreases with the increment of the wavelength of observation. Figures 7e–7h show photonic LDOS maps calculated for the nanorod at the spectral positions (A–D) indicated in Figure 6a. Being consistent with the experimental finding, the number of local maxima decreases toward the longer wavelength. It is to be noted that, while plasmon modes with even numbers of anti-nodes (m_L is even) are dipole-forbidden in the far-field excitation because of their odd-parity characters, these modes are actually allowed under spatially localized excitation in the near-field as seen in Figures 5c, 7b, and 7d.

From the experimental observations described above and those on other rods, we can summarize the relationship between LSP resonances and nanorod dimensions. A gold nanorod with a relatively small aspect ratio (<5) exhibits a transverse and a longitudinal dipolar resonance. The resonance wavelength of the transverse mode is located near 520 nm regardless of the nanorod dimension. The resonance wavelength of the dipolar longitudinal mode ($m_L = 1$) is, on the contrary, strongly dependent on the aspect ratio of the rod. The resonance peak shifts to a longer wavelength as the aspect ratio increases. When the aspect ratio of the nanorod reaches 6, the mode of $m_L = 2$ appears near 600 nm, in addition to the red-shifted dipolar longitudinal mode. With further increase of the aspect ratio, resonance wavelengths of these two modes shift toward a longer wavelength region, and then the $m_L = 3$ mode appears near 600 nm. Appearance of multipolar modes ($m_L > 1$) of the long nanorod is explained in this way.

By plotting the resonance wavelengths/energies of the plasmon modes against the wave vectors of the plasmons, the dispersion relation of the gold nanorods is obtained. The wave vector for the plasmon resonance, $k_{sp} = 2\pi/\lambda_{sp}$ where λ_{sp} is the plasmon wavelength, is estimated directly from the transmission image. Figure 8a shows the dispersion relation obtained from near-field transmission measurements for several nanorods of different lengths with an identical diameter (20 nm).[26,63] The plotted points for rods of different lengths follow approximately a single dispersion curve, as long as the diameter is the same. The dispersion relation based on DOS calculations also follows this curve and converges approximately to the resonance frequency of the transverse plasmon mode at a high wavenumber limit. Although the observed

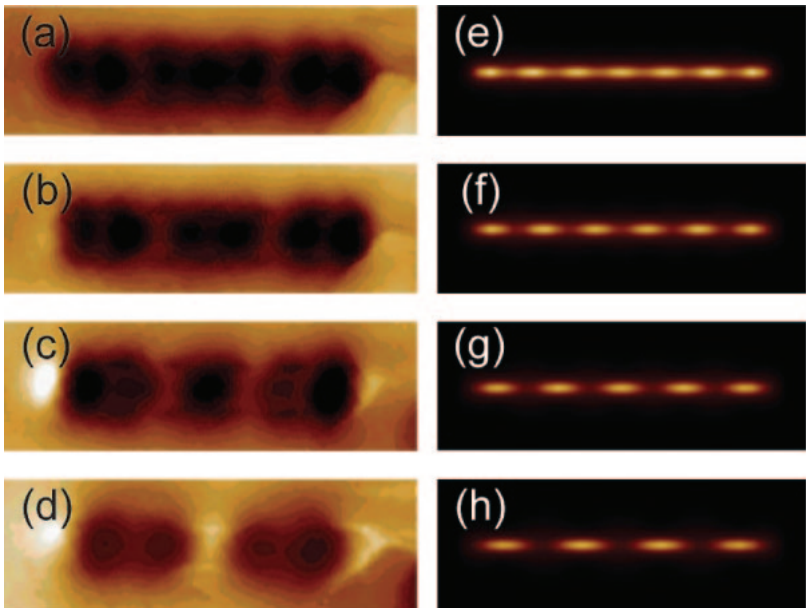

Figure 7. (a–d) Near-field transmission images of a single gold nanorod (diameter 20 nm, length 510 nm). The images were obtained at wavelength regions of (a) 647–666 nm, (b) 666–686 nm, (c) 705–725 nm, and (d) 822–842 nm. (e,f) Simulated LDOS images of a nanorod (diameter 20 nm, length 520 nm). The images were calculated at (e) 636 nm, (f) 679 nm, (g) 722 nm, and (h) 829 nm. Image size of each panel: 220 nm × 700 nm.

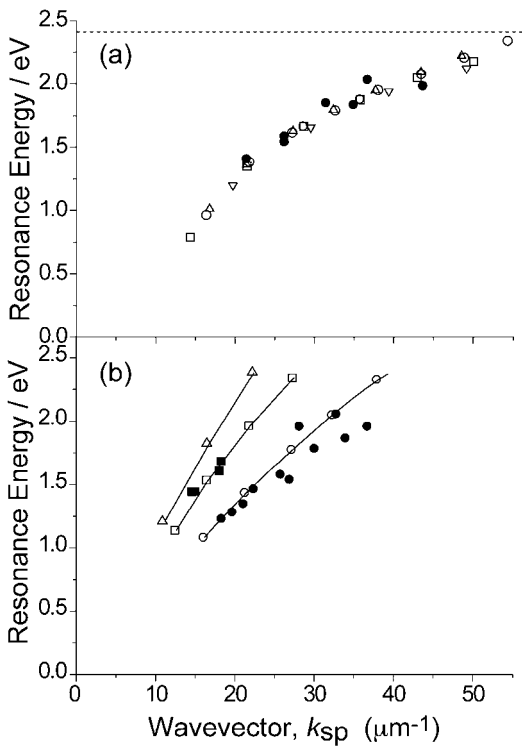

Figure 8. (a) Dispersion relation for single gold nanorods. Closed circles: observations. Open symbols: calculations. Dashed horizontal line indicates the transverse plasmon resonance energy. (b) Dispersion relations of plasmon modes in single gold nanorods. Circles: diameter 20 nm. Squares: diameter 30 nm. Triangles: diameter 40 nm. Closed symbols: observations. Open symbols: calculations. Solid curves are guide to the eyes (Reproduced with permission from Ref. 26. Copyright 2005, American Institute of Physics).

dispersion relation is independent of the length of the nanorod, it does depend strongly on the diameter of the nanorod and is shifted toward a higher energy region with increase of the diameter (Figure 8b). The origin of the shift is ascribed to a depolarization effect in the nanorod. Similar results were also obtained in far-field measurements of gold nanowires fabricated by electron-beam lithography.[64]

7. Near-Field Two-Photon-Induced Photoluminescence Imaging

The excitation process of two-photon-induced PL (TPI-PL) of a given system (such as a molecule and a material) begins with either simultaneous or sequential absorption of two-photons. After that, the initially excited state rapidly relaxes to an emissive state via non-radiative processes. Finally, PL is emitted from the system. For excitation of the TPI-PL, a light source with a very high density of photons such as a pulsed (ps to fs) laser source is required. The shorter the pulse width, the more efficiently the TPI-PL is excited. The TPI-PL intensity increases with the square of the incident power (i.e., forth power of the incident optical field). This is in contrast to the one-photon process, where PL intensity scales linearly with the incident power, and provides an experimental tool with a higher sensitivity to optical fields over the single-photon process.

In the case of gold nanoparticles, TPI-PL can be excited by near-infrared photons (λ = 780–900 nm), and visible PL (λ = 500–800 nm) is radiated. As is typical for TPI-PL, energy of the emitted photon is higher than that of the incident photons, and hence only little background signal is found in the spectral range of the PL. Consequently, we can perform nearly background-free near-field imaging measurements by monitoring the PL. Such near-field TPI-PL imaging technique enables us to visualize optical fields in the vicinity of single gold nano-

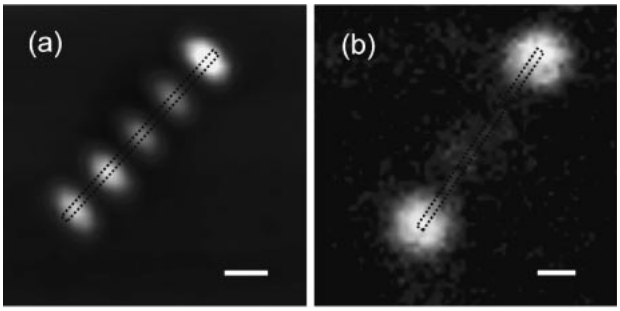

Figure 9. Near-field two-photon excitation images of single gold nanorods detected by two-photon-induced photoluminescence (TPI-PL): Nanorod dimension (diameter × length): (a) 20 nm × 540 nm, (b) 21 nm × 565 nm. Scale bars: 100 nm. Dashed lines indicate approximate shapes of the rods estimated from topography measurements.

particles with high sensitivity. In the following, we present optical characteristics of the TPI-PL and near-field TPI-PL imaging of single gold nanoparticles.

7.1 Single Gold Nanorods. Figure 9a shows a near-field two-photon excitation image of a single gold nanorod. The incident excitation field (wavelength 780 nm) was parallel to the long axis of the nanorod, and TPI-PL in the region between 450 and 650 nm was detected. As is similar to the transmission image, spatial oscillation is observed along the long axis of the nanorod, and is assigned to the spatial feature of the plasmon mode excited by the incident photons. A notable unique characteristic of the TPI-PL image, compared with that of the transmission image in the previous section, is the higher signal contrast of the intensity profile. This is primarily due to the non-linear character of the TPI-PL process.

In some cases, TPI-PL is dominantly excited at both ends of the nanorod as shown in Figure 9b. Excitation efficiency of PL, at a given position on the particle, is proportional to the two-photon absorption probability and also to local electromagnetic field enhancement. The former reflects photonic LDOS (LSP resonance effect) and shows oscillatory pattern along the long axis of the nanorod. The latter originates in two factors, the LSP resonance effect and the lightning rod effect.[65–67] The lightning rod effect is a phenomenon in which electromagnetic field is spatially confined near the sharpest feature of the conductor surface. The effect is determined by the geometrical shape of the nanoparticle, and weakly wavelength-dependent. Electric-field enhancement due to the lightning rod effect preferentially takes place near the sharp edges of the nanorod. By contrast, the enhancement due to the LSP resonance effect can be found at inner parts of the nanorod along the surface of the particle, and is strongly wavelength-dependent. The prominent feature observed in Figure 9a is originated undoubtedly in the LSP effect, while that in Figure 9b may be explained by the lightning rod effect. The relative importance of these two contributions to the field enhancement for each nanorod has not been completely predictable, however. The difference between Figures 9a and 9b may be at least partly attributed to the difference in resonance conditions because of the different sizes. Another possible origin is the difference in microscopic structure (such as defects) of the nanorod. Microscopic defects on the nanorod would hinder formation of LSP waves, and thus the relative significance of the LSP resonance enhancement might be lowered if there are serious defects. Effects of the microscopic defects were also discussed on the plasmon propagation lengths on silver nanowires.[68]

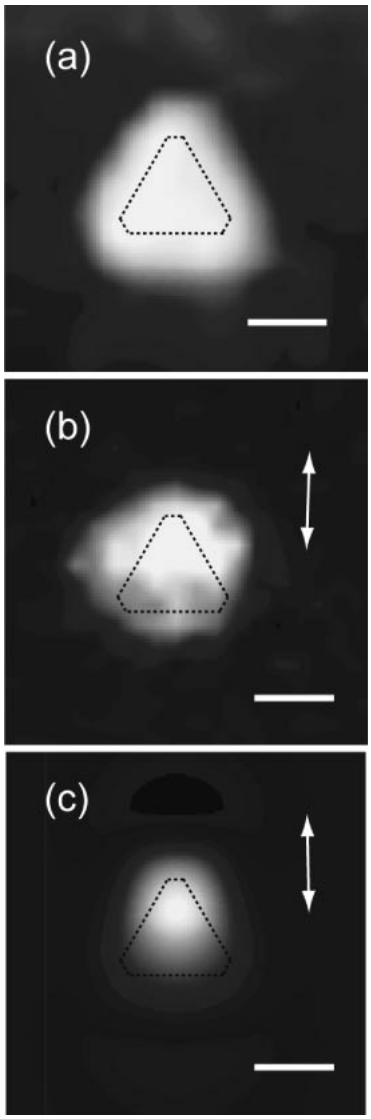

Figure 10. (a) Topography of a single gold triangular nanoplate (thickness 18 nm, base length 160 nm). (b) Two-photon excitation image of the single gold triangle. (c) Calculated electromagnetic field distributions near the triangle. Arrows indicate the direction of the incident polarization. Dashed lines indicate approximate shape of the triangle estimated from (a). Scale bars: 100 nm (Reproduced with permission from Ref. 29. Copyright 2006, American Institute of Physics).

7.2 Single Triangular Nanoplate.[29] The near-field two-photon excitation imaging by TPI-PL is applicable to gold nanoparticles of various shapes. We have measured many kinds of nanoparticles. We have found that gold nanoplates (circular disks, triangles, and so on) in general exhibit intense TPI-PL. The PL from nanoplates is one or two orders of magnitudes stronger than that observed for nanoparticles of other shapes. In Figure 10 is shown a typical example of near-field

observation of a triangular gold nanoplate. Dimensions of the triangle are estimated to be $160 \pm 30\,\text{nm} \times 18 \pm 5\,\text{nm}$ (base length × thickness) from the topography image in Figure 10a. Figure 10b shows the near-field excitation image of the triangle. The excitation probability is found to be localized slightly in the inner part of the triangle near one of the apexes. The electric field calculation (Figure 10c) based on the Green dyadic method reproduces the observed feature well. For electric field (PL intensity) enhancement, both the LSP mechanism and the lightning rod effect are operative, as is similar to the nanorod case. Although the image shows enhanced emission at the inner position of the triangle, which is rather indicative of the LSP mechanism, the dominant factor determining the enhancement is not obvious only from the images in Figures 10b and 10c. As mentioned in the previous subsection, the LSP effects show strong wavelength dependence, while the lightning rod effect depends weakly on the incident wavelength. The observed TPI-PL intensity is found to be strongly wavelength-dependent, and this result suggests that the LSP enhancement is the principal factor that determines the images in Figures 10b and 10c. The TPI-PL image is, therefore, attributed to a LSP mode of the triangle nanoplate. An apex giving the maximum electromagnetic field can be selected among the three equivalent apexes by rotation of the incident polarization. Such a polarization dependency originates from the degenerate character of the two-dimensional LSP wave functions. The polarized light selectively visualizes one of the degenerate plasmon wave functions.

Very recently, plasmon mode imaging of a single triangle silver nanoparticle using electron energy loss spectromicroscopy (EELS) was reported.[69] The method relies on the observation of SPs as resonance peaks in the electron-energy loss spectra. There might be specific properties of plasmon excitations by electrons. Comparison between the SNOM and the EELS measurements will clarify this point.

7.3 Spectroscopic Characteristics of the Photoluminescence. We examined a number of TPI-PL spectra of single gold nanoparticles with different shapes and sizes and found that any PL spectrum of a gold nanoparticle shows two peaks around 550–560 and 630–670 nm (Figure 11), regardless the size and shape of the particle. The intensity ratio of the two peaks varies from particle to particle, but has little correlation with the size and shape of the particle in a systematic way. Photon energies of these spectral bands are comparable to energy separations between the Fermi surface and the d bands near the L and X symmetry points of the Brillouin zone.[70] From these facts, we can describe the PL process as follows. The process begins with sequential two-photon excitation of an electron, from a valence d-band to a conduction sp-band as a whole. After relaxation occurs for the initially excited electron and hole to new energy states via manifold of scattering processes in gold, an electron is created in the conduction band, leaving a hole in the valence band. Finally, emission takes place when the electron and hole recombines. In a gold crystal, optical transition preferentially occurred near the X and L symmetry points, and thus the two peaks observed are assigned to the radiative recombination of the electron–hole pair occurring near these symmetry points. Polarization characteristics of the PL are reflected by the transition moments

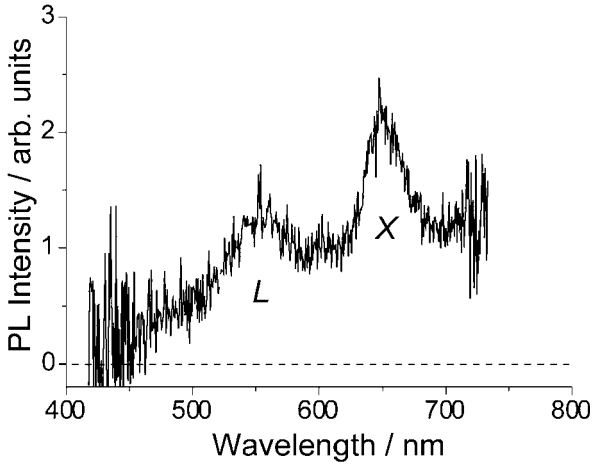

Figure 11. TPI-PL spectrum of a single gold nanorod (Reproduced with permission from Ref. 28. Copyright 2004, American Chemical Society).

of the PL. The observed polarizations of the PL are reasonably understood by considering the crystalline structure of the gold nanoparticle on the basis of the PL mechanism mentioned above.[71] The lifetime of the PL is also consistent with the PL mechanism.

We propose here that TPI-PL from gold nanoparticles is attractive for non-linear optical imaging of biological samples.[72,73] Gold nanoparticles are highly photo-stable and considered to be inactive in biological systems. Excitation by near-infrared photons, where the absorption of water and biological sample are minimized, is also advantageous for this purpose. TPI-PL from gold nanoparticles is hence expected to give a promising tool for bio-imaging.

8. Surface-Enhanced Raman Scattering[74,75]

Raman scattering spectroscopy is a very useful means to identify chemical species. However, very small cross-sections of the Raman processes ($\approx 10^{-29}\,\text{cm}^2$) limit its practical applications. In the mid 1970s, great enhancement of Raman scattering from molecules adsorbed on metal surfaces was reported.[76–78] This effect, known as surface-enhanced Raman scattering (SERS), renders Raman analysis tractable in a variety of applications.[79,80] SERS is especially of great significance when the SP resonance of the metal is excited. Under coexistence of noble metal nanoparticles, Raman scattering enhancement of several orders of magnitudes is obtained. Further huge enhancement (10^{11}–10^{14}) was attained in the late 1990s.[81–83] The Raman cross-section in this case ($\approx 10^{-16}\,\text{cm}^2$) is comparable to the typical fluorescence cross-section of a dye molecule. Such a huge enhancement allows us to perform vibrational spectroscopy with single molecule sensitivity, and is greatly advantageous for many practical applications.

A number of studies were performed to reveal the origin of the enhancement. From these studies, it becomes evident that aggregation of the noble metal particles is essential for single-molecule sensitivity in SERS. The dimer of the spherical particles is sometimes considered as the simplest model system to examine the effects of aggregation in ultrasensitive SERS.[84,85] Figure 12 illustrates electromagnetic field distribu-

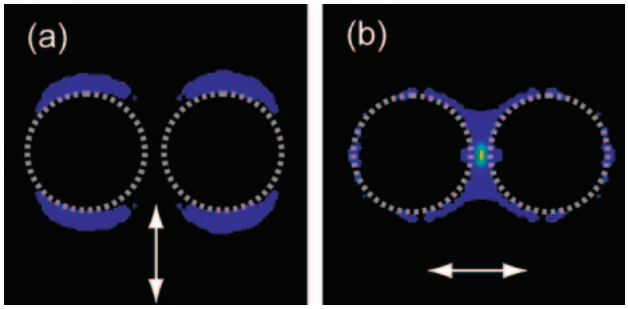

Figure 12. Calculated electromagnetic field distributions of a dimer of spherical gold nanoparticles (diameter 100 nm, dashed circles) excited by incident wavelength of 780 nm. Gap distance between the particles is 5 nm. Arrows indicate the direction of the incident polarization.

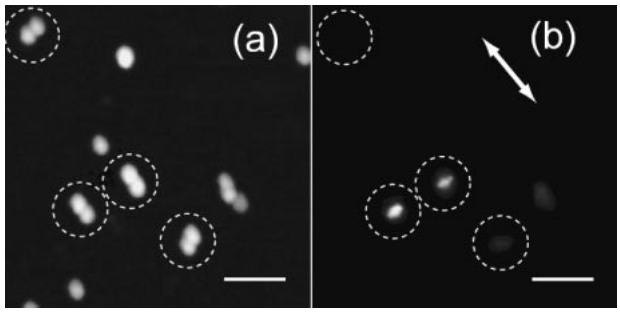

Figure 13. (a) Topography of aggregated and isolated gold nanoparticles. (b) Two-photon excitation image taken with the incident polarization direction indicated by the arrow. Dimers are enclosed by white dotted circles. Scale bars: 500 nm (Reproduced with permission from Ref. 75. Copyright 2005, The Chemical Society of Japan).

tions of the gold nanospheres dimer calculated for two incident-polarization cases. The result of calculation predicts a strongly amplified electromagnetic field at the interstitial site (gap) of the dimer, only when the incident field is parallel to the interparticle axis. The field enhancement factor at the gap is as high as 10^3.

Rigorous examination of the role of the gap is possible if the interstitial site is spatially resolved from the other parts of the aggregate in optical measurements. Linear- and non-linear near-field methods open the door towards such observations of aggregate systems, since the techniques allow us to measure topography and electromagnetic-field distribution simultaneously with sufficient spatial resolution. In this section, we show observations of spatial distributions of electromagnetic field enhancement for dimeric aggregates of gold nanospheres, and discuss the enhancement mechanism of ultrasensitive SERS.

Dimers of gold spherical nanoparticles are prepared by self-assembling the nanoparticles on a cover-slip. Figure 13a shows typical topography of a sample. Dimers and trimers are clearly visible. From the topography and SEM observations, the particles in the aggregate (dimer and trimer) were found being not in direct contact, but separated by several nanometers. The gap distance is scattered from 1 to 10 nm, depending on the dimer. Figure 13b shows TPI-PL images of single gold particles and aggregates. The aggregates (dimers) exhibit intense TPI-PL compared to the isolated single particles. Close inspection of the topography and the TPI-PL images reveal that the intense PL is highly localized at the interstitial sites of the dimers. Moreover, the PL at the interstitial site is strongly dependent on the incident polarizations. The PL is highly enhanced when the incident polarization is parallel to the dimer axis, whereas it gives the minimum intensity when the incident polarization is perpendicular to the axis. These observations are well associated with the calculations shown in Figure 12. In the dimer, excitation of the LSP induces a polarization on each particle. As the opposite charges of the polarizations are facing at the interstitial site when the incident radiation field is parallel to the axis of the dimer, Coulombic interaction occurs in the small-distance gap and creates greatly amplified electromagnetic field. On the other hand, when the incident field is polarized across the interparticle axis, individual LSP on the dimer does not interact with each other through the gap. As a result, the amplitude of electromagnetic field remains comparable to that for the isolated particles.

To investigate the SERS activity in the aggregate, Raman active dye molecules were spin-coated onto the gold-aggregate sample (Figure 14a). Estimated number density of dye molecules was 10–100 per square of 100 nm assuming homogeneous distribution on the substrate. Aperture size of the near-field probe was ca. 50 nm in diameter, and thus several tens of molecules were excited under the aperture of the probe. We excited the Raman scattering by incident wavelength of 785 nm. Raman scattering spectra taken at the probe position on a dimer and on an isolated single gold nanoparticle are shown in Figure 14c. Very intense Raman scattering from the dye molecules are observed at the dimer while there are no detectable signals at the isolated nanoparticle. This result indicates that the dimers enhance the Raman activity in a similar way to TPI-PL. In the scanned area, Raman intensity at the dimer is seriously different for each pair, indicating that the detailed structure of the dimer, the gap distance in particular, is an important factor for Raman enhancement. Raman intensity is also strongly dependent on the incident polarization in the same manner as observed in the TPI-PL measurement: the Raman intensity is enhanced when the incident field is polarized parallel to the interparticle axis of the dimer. This behavior is again in accordance with the TPI-PL case. The observed spectral positions of the near-field excited Raman bands do not vary substantially from the corresponding ones in the far-field excited spectra, and are assignable to vibrational modes of the dye molecules.[86,87] The small differences in band positions between the near-field and the far-field excited spectra are attributable to the interaction between the adsorbed molecule and gold nanoparticles. Spectral fluctuations in a time scale of seconds are found for band intensities and positions. The origin of the fluctuation may be ascribed to lateral motion (diffusion) of molecules on the substrate and/or changes in adsorption geometry. The result suggests that the near-field excited Raman scattering signal is arising from quite a small number of molecules.

Raman active sites are visualized by monitoring the Raman band intensity near 1600 cm^{-1} as shown in Figure 14d. The images again depend on the direction of the incident polarization. Namely, Raman scattering is enhanced when the incident

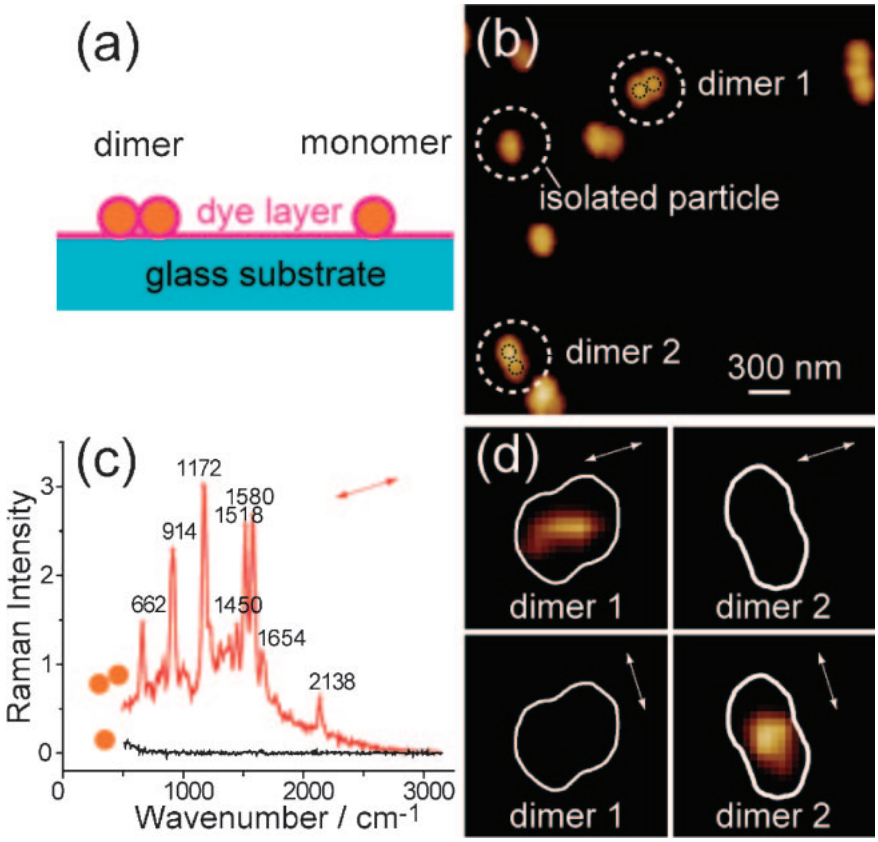

Figure 14. (a) Schematic illustration of the sample for Raman measurements. See the text. (b) Topography of aggregated and isolated gold nanoparticles. (c) Near-field excited Raman spectra of dimer 1 and of an isolated particle indicated in (b). (d) Near-field Raman excitation images of dimer 1 and dimer 2 obtained for the bands near 1600 cm^{-1}. The images were measured at different incident polarizations indicated by the arrows. White curves indicate approximate shape of the dimers. Image size of each panel: 540 nm × 540 nm (Reproduced with permission from Ref. 74. Copyright 2006, American Chemical Society).

field is parallel to the interparticle axis while no Raman enhancement is found when the incident field is perpendicular to the dimer axis. The enhanced excitation probability of the Raman scattering is highly localized at the interstitial site of the particles. We also found that Raman scattered photons are preferentially polarized along the interparticle axis of the dimer, indicating the importance of the local electromagnetic field at the interstitial site in the dimer. These results correspond with those of the TPI-PL measurements and are consistent with the theoretical prediction for the dimer model (Figure 12). It is theoretically predicted that the dimer plasmon shows a resonance around 800 nm for a dimer of ca. 100-nm diameter gold nanospheres, depending on the gap distance between the particles.[84] This means that the Raman scattering can be greatly enhanced by using a near-infrared excitation light source. The maximum enhancement is estimated as high as 10^{11} in this case. Our experimental observation using an excitation source at 785 nm shows that the maximum Raman enhancement actually reaches $10^{10–11}$ assuming homogeneous distribution of the dye molecules. This result also supports the electromagnetic mechanism of enhancement of the dimer model. These observations give a clear proof that the amplified electromagnetic field at the interstitial site in the dimer is one of the most crucial factors in SERS with single-molecule-level sensitivity. The near-field observation of the SERS active materials may provide a valuable tool to reveal the mechanism of enhancements and to design efficient SERS-active substrates and materials.

9. Ultrafast Transient Imaging[27,88]

Elucidation of ultrafast dynamics in metal nanoparticles and their spatial position dependencies is indispensable when we utilize nanoparticles as basic elements of ultrafast electronic and optical devices. The dynamic behavior of conduction electrons in metal nanoparticles is intrinsically reflected in device performance.[89,90] For instance, dynamic processes of electron–electron and electron–phonon scattering lead to ultrafast thermalization of the conduction electrons, resulting in changes of optical properties and electric resistance/conductance of the metal nanoparticle. In metal nanoparticles, the particle size becomes comparable to the mean free path of the conduction electrons, and hence electron-surface scattering may have a certain influence on these dynamic processes. However, such influence of particle boundaries on the dynamics has been little characterized in a space-resolved manner. To achieve high performance of the devices, understanding dynamic features of the electrons with high spatial resolution is essential.

In view of dynamic studies, time-resolved methods undoubtedly give the most direct information. Most of the time-resolved studies on metal nanoparticles have focused on, however, the size and shape dependences of dynamic processes by using macroscopic ensembles of nanoparticles.[91–94]

It is hard to reveal details of the dynamic processes of nanoparticles, because of the size and shape distribution of the nanoparticles in the ensemble measurements. To gain direct access to ultrafast dynamics in nanoparticles, time-resolved microscopy, which enables observation of individual single particles, gives the most promising tool. Various kinds of single-nanoparticle spectroscopy using confocal optical microscopes become feasible, and allow us to obtain valuable information on electron dynamics and non-linearities of the nanoparticles.[95–99] The spatial resolution in this case is limited, however, by the diffraction limit of light. Hence, the dynamic processes observed are spatially averaged over the particle volume. In contrast, near-field optical microscopy enables visualization of electromagnetic field distribution in real space with a spatial resolution not limited by the diffraction. By combining the near-field method with time-resolved techniques, ultrafast near-field imaging becomes possible and enables us to visualize time-resolved images beyond the diffraction limit of light.[27] The methods open up detailed analysis of the ultrafast optical/physical processes in the nanoparticles. In this section, we discuss ultrafast dynamics of single gold nanorods, based on ultrafast near-field measurements. We analyze the transient images of the nanorod obtained and discuss the origin of the characteristics transient behavior.

The result of ultrafast near-field measurements on a single gold nanorod (diameter 30 nm, length 300 nm) is illustrated as a typical sample. The gold nanorod shows two longitudinal LSP resonance peaks near 620 and 750 nm, and are assigned to $m_L = 3$ and $m_L = 2$ modes, respectively, based on the near-field transmission measurements and theoretical calculations. The peak wavelength of the fundamental dipolar mode ($m_L = 1$) is estimated by the calculation to be ≈1700 nm. In the transient transmission measurements, a sequence of near infrared (wavelength 780 nm) pulses is used, to photo-excite (pump) the nanorod and then to observe (probe) the dynamic processes after the photoexcitation. In this scheme, the pump pulse perturbs the electron distribution of conduction band, and energy dissipation processes such as electron–electron and electron–phonon scattering are detected through a transient transmission intensity change as a function of pump–probe delay time. At the excitation wavelength, both the dipolar longitudinal LSP mode (resonance peak at $\lambda_{LSP} > 1\,\mu m$) and the second LSP mode ($\lambda_{LSP} = 750$ nm) are excited. The observed transient transmission images of the nanorod are shown in Figure 15. Bright and dark parts correspond to induced and bleached absorption regions, respectively. Interestingly, both induced and bleached absorptions are observed simultaneously in the single nanorod.

To gain insight into the origin of characteristic features of the observed image, we tried to simulate the transient transmission images by taking the electronic temperature rise in the nanorod induced by photoexcitation into consideration. We assume a spatially uniform electronic temperature rise at a delay time of several hundred femtoseconds. Ultrafast measurements of thin gold films (up to ≈300 nm) showed that the heat transport velocity in the direction normal to the surface is $\approx 10^8\,cm\,s^{-1}$.[100] If electronic heat transport in the nanorods is as fast as that in the thin films, the electrons in the rod (length 300 nm) may be thermally equilibrated within 600 fs.

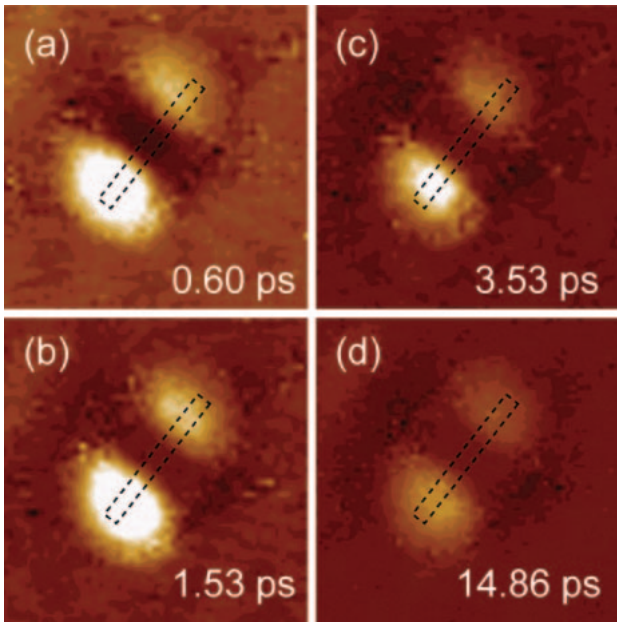

Figure 15. Transient transmission images of a single gold nanorod (diameter 30 nm, length 300 nm) taken at several pump–probe delay times. The delay time is indicated in each image. Image size of each panel: 600 nm × 600 nm.

It has been established, as already described in Section **6**, that steady-state transmission images are well reproduced by photonic LDOS. Based on that result, we assume that the transient transmission change ($\Delta I_{transient}$) is given by a variation of LDOS due to the elevation of electronic temperature in the nanorod upon photoexcitation. The transient image is thus simulated by

$$\Delta I_{transient}(\vec{r}, \omega, T_{elec}, \Delta T_{elec}) \propto \rho(\vec{r}, \omega, T_{elec} + \Delta T_{elec}) - \rho(\vec{r}, \omega, T_{elec}), \quad (3)$$

where ΔT_{elec} denotes elevation of electronic temperature. In eq 3, the temperature dependence of LDOS arises from dielectric-constant (ε) change of the material. The dielectric constant at the elevated temperature ($T_{elec} + \Delta T_{elec}$) was evaluated by taking the joint density-of-states in gold and the temperature dependence of electron distribution near the Fermi surface into account.[101] We found that the imaginary part of the dielectric constant remains constant at the probe wavelength ($\lambda =$ 780 nm) while the absolute value of the real part (negative value) becomes larger with increment of ΔT_{elec}.

We first carried out simulations of DOS spectra (spatially integrated) of a nanorod at various temperatures, to understand the effect of temperature rise on plasmon resonances. Figure 16b shows the simulated DOS spectra of a gold nanorod at two temperatures: at room temperature ($T_{elect} =$ 300 K) and at elevated temperature (600 K). The result indicates that the increment of the temperature induces a red-shift of the LSP resonance and an increase in DOS of the nanorod at the probe wavelength (780 nm). Induced absorption as a spatial average is therefore expected for the nanorod.

Now, we simulate a transient image based on eq 3, from the LDOS calculated at the two temperatures. Figure 16c shows the simulated transient image. Bright and dark parts indicate

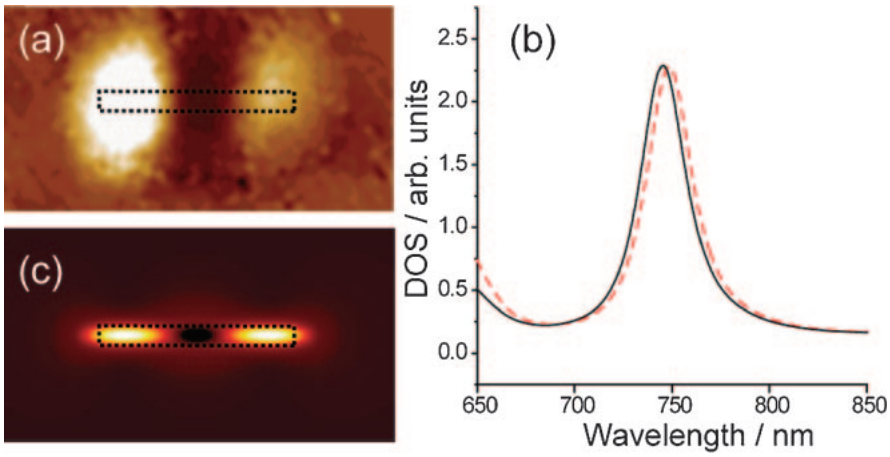

Figure 16. (a) Near-field transient transmission image (decay time 0.6 ps) of the nanorod taken from Figure 15. (b) Calculated density-of-states spectra of the single gold nanorod (diameter 30 nm, length 300 nm) at room temperature (300 K, dashed curve) and at the elevated temperature (600 K, solid curve). (c) Simulated transient transmission image for the single gold nanorod. Dotted squares indicate approximate shapes of the gold nanorod (Reproduced with permission from Ref. 88. Copyright 2008, the American Physical Society).

the enhancement and reduction regions of the LDOS, respectively. The simulated result qualitatively reproduces the observed transient image at 0.6 ps (Figure 16a). On closer inspection of the simulated results, it is revealed that the induced absorption at both ends and the bleached absorption at the central part are attributed to enhancement of the second plasmon mode ($m_L = 2$) and reduction of the dipolar mode ($m_L = 1$), respectively. The characteristic feature observed in the transient image is thus assignable to the LDOS change due to the elevation of electronic temperature in the nanorod. We also investigated transient images of single gold nanorods with different lengths and diameters. Observed transient images are found to show spatial feature characteristic of the nanorod dimensions studied, and are ascribed in a unified manner to the changes of LDOS due to the elevation of electronic temperature upon photoexcitation.

Next we focus on temporal (dynamic) response in the nanorod. As is seen in Figure 15, temporal response at the central part of the particle is different from that at the ends. Figure 17 shows time responses observed at representative positions indicated as 1 to 5 in the inset of the figure. A fast rise and a slow decay are seen in the nanorod, except for the central part. The time responses can be fitted by double-exponential functions as summarized in Table 1. The relaxation process after photoexcitation of a gold nanoparticle is considered as follows. The energy of the photon is first converted to electronic excitation energy, and is then dissipated to other electrons via electron–electron scattering. The excitation energy is further dissipated to other degrees of freedom by electron–phonon scattering in the particle and finally into the surrounding medium by phonon–phonon scattering. The fast (0.6 ps) and slow (1.5–2.5 ps) decay components obtained in the present experiment are assigned to electron–electron and electron–phonon scattering processes, respectively. At the center of the rod, the electron–phonon scattering process is apparently absent probably because the signal arising from that is hidden in the tail of the decay signal due to the electron–electron scattering. From the table, it becomes evident that the energy dissipation pro-

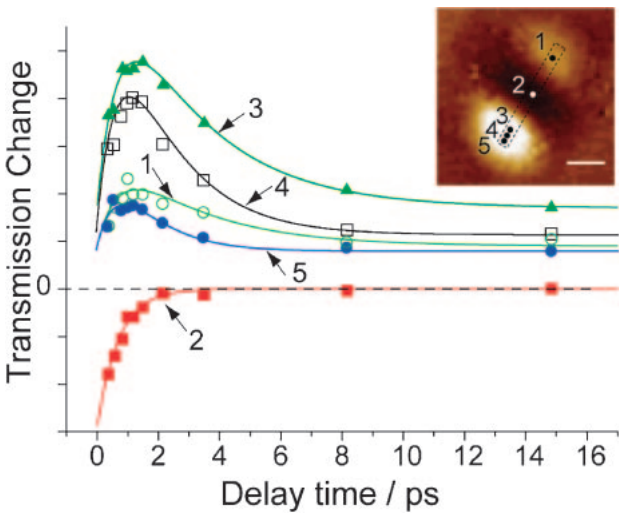

Figure 17. Transient transmission changes measured for the gold nanorod as functions of delay time, converted from the data in Figure 15. Solid curves indicate double (for positions 1, 3, 4, and 5) and single (for position 2) exponential fits, respectively. Inset: analyzed positions on the nanorod. Dotted square indicates an approximate shape of the gold nanorod (Reproduced with permission from Ref. 27. Copyright 2004, American Chemical Society).

Table 1. Parameters Obtained from Double-Exponential Fits of Time Responses in the Nanorod

Position	τ_{fast}/ps	τ_{slow}/ps
1	0.6	2.8
2	0.6	—
3	0.6	2.8
4	0.6	1.8
5	0.6	1.5

cess is dependent on the position on the nanorod in a spatial scale of tens of nanometers. Notably, the decay time of the electron–phonon process becomes faster toward the end edge of the nanorod. The spatial scale of the position dependence is close to the mean-free-path of the conduction electrons (≈30–40 nm for gold). From the measurements of various single gold nanorods, we have also found that energy dissipation processes are dependent on the nanorod dimensions. Considering these facts and the large surface/volume ratio near the edge of the nanorod, the observed position dependence of the electron–phonon process is possibly related to electron-surface scattering in the electron–phonon process. On the other hand, far-field ultrafast studies have shown that the size and shape dependence of the electron–phonon scattering is significant only for smaller particles (<10 nm),[91–93] which is contradictory to the interpretation above. Further investigations are underway to clarify the origin of the position dependence of the electron–phonon process.

10. Concluding Remarks

We have shown here the development of new methods of near-field microspectroscopy and applications to nanomaterials. The developed microscope can carry out linear and nonlinear spectroscopic measurements and achieves high spatial resolution as well as high time resolution. In this review, we focused on the optical properties of plasmonic materials (metal nanoparticles). We demonstrated visualizations of spatial features of the plasmon wave functions and optical fields on the nanoparticles, and of the ultrafast time response. The near-field methods allow us to provide new insights into optical properties of plasmonic materials, and the knowledge obtained through the near-field methods also provides valuable information for a variety of applications of plasmon-related and other nanomaterials, such as chemical- and bio-sensors, waveguides, nano-optical devices, etc. The localized plasmon may achieve photoexcitation of molecules that is not accessible by conventional far-field excitation in the dipole approximation, and may provide new schemes in photochemistry. This characteristics as well as enhanced optical fields may open up a new research field in chemistry.

Although the near-field methods described here have great potential for fundamental as well as applied sciences, there are still numerous issues that need to be overcome for universal application. For instance, to gain precise understanding of near-field images, development of numerical simulation methods for realistic experimental configurations (including the tip-sample interaction) is highly desirable. From the experimental point of view, tip performance such as transmission throughput, tip stability, and photo-damage threshold should be improved. Micromachining processes and new tip concepts are promising to get high-performance near-field probes. For ultrafast measurements, higher time resolution is also desired. We are currently trying to get a time-resolution close to or higher than the dephasing time of the plasmons at the near-field probe tip. Having relevant techniques all together, we may develop highly advanced near-field spectroscopic methods, which are attractive and reliable in a wide research area of chemistry and physics. The method also provides a basis for manipulations of the excitation dynamics and optical functionality of nanomaterials at the nanometer scale. Optical control of plasmon waves would be particularly attractive particularly when the materials are utilized for applications in optical elements and photochemical reactions.

The authors would like to thank to Drs T. Nagahara, J. K. Lim, N. Horimoto, M. K. Hossain, and Professor M. Kitajiama for their many and essential contributions to this work. The authors also thank the Equipment Development Center of IMS for collaboration in construction of the SNOM apparatus. This work was supported by Grants-in-Aid for Scientific Research (Grant Nos. 16350015, 16750017, 17655011, 17034062, 18205004, 18685003, and 19049015) from the Japan Society for the Promotion of Science and from the Ministry of Education, Culture, Sports, Science and Technology.

References

1 H. Okamoto, K. Imura, *J. Mater. Chem.* **2006**, *16*, 3920.
2 E. Abbe, *Arch. Mikrosk. Anat. Entwicklungsmech.* **1873**, *9*, 413.
3 M. Born, E. Wolf, *Principles of Optics*, Cambridge University Press, Cambridge, **1999**.
4 E. A. Ash, G. Nicholls, *Nature* **1972**, *237*, 510.
5 D. W. Pohl, W. Denk, M. Lanz, *Appl. Phys. Lett.* **1984**, *44*, 651.
6 U. Durig, D. W. Pohl, F. Rohner, *J. Appl. Phys.* **1986**, *59*, 3318.
7 E. Betzig, J. K. Trautman, T. D. Harris, J. S. Weiner, R. L. Kostelak, *Science* **1991**, *251*, 1468.
8 L. Novotony, B. Hecht, *Principle of Nano-optics*, Cambridge University Press, Cambridge, **2006**.
9 K. Imura, H. Okamoto, *J. Spectrosc. Soc. Jpn.* **2006**, *55*, 161.
10 K. Imura, *Mol. Sci.* **2007**, *1*, A0006.
11 N. Bloembergen, *Nonlinear Optics*, World Scientific, Singapore, **1996**.
12 U. Kreibig, M. Vollmer, *Optical Properties of Metal Clusters*, Springer-Verlag, Berlin, **1995**.
13 M. Kerker, *The Scattering of Light and Other Electromagnetic Radiation*, Academic Press, New York, **1969**.
14 S. Kawata, *Near-field Optics and Surface Plasmon Polaritons*, Springer-Verlag, Berlin, **2001**.
15 R. H. Ritchie, *Surf. Sci.* **1973**, *34*, 1.
16 K. Li, M. I. Stockman, D. J. Bergman, *Phys. Rev. Lett.* **2002**, *91*, 227402.
17 E. Hao, G. C. Schatz, *J. Chem. Phys.* **2004**, *120*, 357.
18 J. R. Lakowicz, *Anal. Biochem.* **2005**, *337*, 171.
19 S. A. Maier, M. L. Brongersma, P. G. Kik, S. Meltzer, A. A. G. Requicha, H. A. Atwater, *Adv. Mater.* **2001**, *13*, 1501.
20 W. L. Barnes, A. Dereux, T. W. Ebbesen, *Nature* **2003**, *424*, 824.
21 E. Ozbay, *Science* **2006**, *311*, 189.
22 K. Cho, *Optical Response of Nanostructures*, Springer-Verlag, Tokyo, **2004**.
23 K. Cho, Y. Ohfuti, K. Arima, *Surf. Sci.* **1996**, *363*, 378.
24 K. Imura, T. Nagahara, H. Okamoto, *Chem. Phys. Lett.* **2004**, *400*, 500.
25 T. Nagahara, K. Imura, H. Okamoto, *Rev. Sci. Instrum.* **2004**, *75*, 4528.
26 K. Imura, T. Nagahara, H. Okamoto, *J. Chem. Phys.* **2005**,

122, 154701.
27 K. Imura, T. Nagahara, H. Okamoto, *J. Phys. Chem. B* **2004**, *108*, 16344.
28 K. Imura, T. Nagahara, H. Okamoto, *J. Am. Chem. Soc.* **2004**, *126*, 12730.
29 K. Imura, T. Nagahara, H. Okamoto, *Appl. Phys. Lett.* **2006**, *88*, 023104.
30 K. Ueno, S. Juodkazis, M. Mino, V. Mizeikis, H. Misawa, *J. Phys. Chem. C* **2007**, *111*, 4180.
31 L. Yin, V. K. Vlasko-Vlasov, J. Pearson, J. M. Hiller, J. Hua, U. Welp, D. E. Brown, C. W. Kimball, *Nano Lett.* **2005**, *5*, 1399.
32 Y. Sun, Y. Xia, *Science* **2002**, *298*, 2176.
33 J. Turkevich, P. C. Stevenson, J. Hiller, *Discuss. Faraday Soc.* **1951**, *11*, 55.
34 C. J. Murphy, T. K. Sau, A. M. Gole, C. J. Orendorff, J. Gao, L. Gou, S. E. Hunyadai, T. Li, *J. Phys. Chem. B* **2005**, *109*, 13857.
35 F. Kim, J. H. Song, P. Yang, *J. Am. Chem. Soc.* **2002**, *124*, 14316.
36 B. Nikoobakht, M. A. El-Sayed, *Chem. Mater.* **2003**, *15*, 1957.
37 Y. Niidome, K. Nishioka, H. Kawasaki, S. Yamada, *Chem. Commun.* **2003**, 2376.
38 N. R. Jana, L. Gearheart, C. J. Murphy, *J. Phys. Chem. B* **2001**, *105*, 4065.
39 B. D. Busbee, S. O. Obare, C. J. Murphy, *Adv. Mater.* **2003**, *15*, 414.
40 S. A. Maier, H. A. Atwater, *J. Appl. Phys.* **2005**, *98*, 011101.
41 R. Jin, Y. C. Cao, E. Hao, G. S. Métraux, G. C. Schatz, C. A. Mirkin, *Nature* **2003**, *425*, 487.
42 S. Link, M. B. Mohamed, M. A. El-Sayed, *J. Phys. Chem. B* **1999**, *103*, 3073; S. Link, M. A. El-Sayed, *J. Phys. Chem. B* **2005**, *109*, 10531.
43 J. E. Millstone, S. Park, K. L. Shuford, L. Qin, G. C. Schatz, C. A. Mirkin, *J. Am. Chem. Soc.* **2005**, *127*, 5312.
44 G. Mie, *Ann. Phys.* **1908**, *330*, 377.
45 C. F. Bohren, D. R. Huffman, *Absorption and Scattering of Light by Small Particles*, Wiley, New York, **1998**.
46 E. H. Synge, *Philos. Mag.* **1928**, *6*, 356.
47 M. Ohtsu, *Near-Field Nano/Atom Optics and Technology*, Springer-Verlag, **1998**.
48 N. Hosaka, T. Saiki, *Opt. Rev.* **2006**, *13*, 262.
49 T. Taubner, R. Hillenbrand, K. Keilmann, *Appl. Phys. Lett.* **2004**, *85*, 5064.
50 J. M. Gerton, L. A. Wade, G. A. Lessard, Z. Ma, S. R. Quake, *Phys. Rev. Lett.* **2004**, *93*, 180801.
51 W. Schade, J. Preusser, D. L. Osborn, Y. Y. Lee, J. deGouw, S. R. Leone, *Opt. Commun.* **1999**, *162*, 200.
52 S. Smith, N. Christian, R. Holme, B. Orr, R. Kopelman, T. Norris, *Ultramicroscopy* **1998**, *71*, 213.
53 A. Nilius, T. W. Wallis, W. Ho, *Science* **2002**, *297*, 1853.
54 M. F. Crommie, C. P. Lutz, D. M. Eigler, *Nature* **1993**, *363*, 524.
55 E. N. Economou, *Green's Function in Quantum Physics*, Springer-Verlag, Berlin, **1983**.
56 C. Girard, *Rep. Prog. Phys.* **2005**, *68*, 1883.
57 C. Girard, A. Dereux, *Rep. Prog. Phys.* **1996**, *59*, 657.
58 J.-J. Greffet, R. Carminati, *Prog. Surf. Sci.* **1997**, *56*, 133.
59 P. M. Morse, H. Feshbash, *Methods of Theoretical Physics*, McGraw-Hill, New York, **1953**.
60 B. Hecht, H. Bielefeldt, Y. Inouye, D. W. Pohl, L. Novotny, *J. Appl. Phys.* **1997**, *81*, 2492.
61 K. Imura, H. Okamoto, *Opt. Lett.* **2006**, *31*, 1474.
62 L. J. Richter, C. E. Jordan, R. R. Cavanagh, G. W. Bryant, A. Liu, S. J. Stranick, C. D. Keating, M. J. Natan, *J. Opt. Soc. Am. A* **1999**, *16*, 1936.
63 J. K. Lim, K. Imura, T. Nagahara, S. K. Kim, H. Okamoto, *Chem. Phys. Lett.* **2005**, *412*, 41.
64 G. Schider, J. R. Krenn, A. Hohenau, H. Ditlbacher, A. Leitner, F. R. Aussenegg, W. L. Schaich, I. Puscasu, B. Monacelli, G. Boreman, *Phys. Rev. B* **2003**, *68*, 155427.
65 J. I. Gersten, *J. Chem. Phys.* **1980**, *72*, 5779.
66 J. Gersten, A. Nitzan, *J. Chem. Phys.* **1980**, *73*, 3023.
67 P. F. Liao, A. Wokaun, *J. Chem. Phys.* **1982**, *76*, 751.
68 H. Ditlbacher, A. Hohenau, D. Wagner, U. Kreibig, M. Rogers, F. Hofer, F. R. Aussenegg, J. R. Krenn, *Phys. Rev. Lett.* **2005**, *95*, 257403.
69 J. Nelayah, M. Kociak, O. Stephan, F. J. Garcia de Abajo, M. Tence, L. Henrard, D. Taverna, I. Pastoriza-Santos, L. M. Liz-Marzan, C. Colliex, *Nat. Phys.* **2007**, *3*, 348.
70 R. Rosei, *Phys. Rev. B* **1974**, *10*, 474.
71 K. Imura, T. Nagahara, H. Okamoto, *J. Phys. Chem. B* **2005**, *109*, 13214.
72 H. Wang, T. B. Huff, D. A. Zweifel, W. He, P. S. Low, A. Wei, J.-X. Cheng, *Proc. Natl. Acad. Sci. U.S.A.* **2005**, *102*, 15752.
73 N. J. Durr, T. Larson, D. K. Smith, B. A. Korgel, K. Sokolov, A. Ben-Yakar, *Nano Lett.* **2007**, *7*, 945.
74 K. Imura, H. Okamoto, M. K. Hossain, M. Kitajima, *Nano Lett.* **2006**, *6*, 2173.
75 K. Imura, H. Okamoto, M. K. Hossain, M. Kitajima, *Chem. Lett.* **2006**, *35*, 78.
76 M. Fleischmann, P. J. Hendra, A. J. McQuillan, *Chem. Phys. Lett.* **1974**, *26*, 163.
77 D. Jeanmaire, R. P. Van Duyne, *J. Electroanal. Chem.* **1977**, *84*, 1.
78 M. G. Albrecht, J. A. Creighton, *J. Am. Chem. Soc.* **1977**, *99*, 5215.
79 G. C. Schatz, R. P. Van Duyne, *Handbook of Vibrational Spectroscopy*, Wiley, **2002**.
80 M. Moskovits, *Rev. Mod. Phys.* **1985**, *57*, 783.
81 S. Nie, S. R. Emory, *Science* **1997**, *275*, 1102.
82 K. Kneipp, Y. Wang, H. Kneipp, L. T. Perelman, I. Itzkan, R. R. Dasari, M. S. Feld, *Phys. Rev. Lett.* **1997**, *78*, 1667.
83 A. M. Michaels, M. Nirmal, L. E. Brus, *J. Am. Chem. Soc.* **1999**, *121*, 9932.
84 H. Xu, J. Aizpurua, M. Käll, P. Apell, *Phys. Rev. E* **2000**, *62*, 4318.
85 C. E. Talley, J. B. Jackson, C. Oubre, N. K. Grady, C. W. Hollars, S. M. Lane, T. R. Huser, P. Nordlander, N. J. Halas, *Nano Lett.* **2005**, *5*, 1569.
86 A. M. Schwartzberg, C. D. Grant, A. Wolcott, C. E. Talley, T. R. Huser, R. Bogomolni, J. Z. Zhang, *J. Phys. Chem. B* **2004**, *108*, 19191.
87 H. Watanabe, N. Hayazawa, Y. Inouye, S. Kawata, *J. Phys. Chem. B* **2005**, *109*, 5012.
88 K. Imura, H. Okamoto, *Phys. Rev. B* **2008**, *77*, 041401(R).
89 W. L. Barnes, A. Dereux, T. W. Ebbesen, *Nature* **2003**, *424*, 824.
90 E. Ozbay, *Science* **2006**, *311*, 189.
91 S. Link, M. A. El-Sayed, *J. Phys. Chem. B* **1999**, *103*, 8410.

92 J. H. Hodak, A. Henglein, G. V. Hartland, *J. Phys. Chem. B* **2000**, *104*, 9954.
93 C. Voisin, D. Christofilos, P. A. Loukakos, N. Del Fatti, F. Vallée, J. Lermé, M. Gaudry, E. Cottancin, M. Pellarin, B. Broyer, *Phys. Rev. B* **2004**, *69*, 195416.
94 J.-Y. Bigot, V. Halte, J.-C. Merle, A. Daunois, *Chem. Phys.* **2000**, *251*, 181.
95 D. Boyer, P. Tamarat, A. Maali, B. Lounis, M. Orrit, *Science* **2002**, *297*, 1160.
96 M. A. van Dijk, M. Lippitz, M. Orrit, *Phys. Rev. Lett.* **2005**, *95*, 267406.
97 O. L. Muskens, N. Del Fatti, F. Vallée, *Nano Lett.* **2006**, *6*, 552.
98 A. Bouhelier, R. Bachelot, G. Lerondel, S. Kostcheev, P. Royer, G. P. Wiederrecht, *Phys. Rev. Lett.* **2005**, *95*, 267405.
99 M. Pelton, M. Liu, S. Park, N. F. Scherer, P. Guyot-Sionnest, *Phys. Rev. B* **2006**, *73*, 155419.
100 S. D. Brorson, J. G. Fujimoto, E. P. Ippen, *Phys. Rev. Lett.* **1987**, *59*, 1962.
101 M. Guerrisi, R. Rosei, P. Winsemius, *Phys. Rev. B* **1975**, *12*, 557.

Award recipient

Kohei Imura is an assistant professor at Institute for Molecular Science. He received B.S. and M.S. degrees from Department of Chemistry, Faculty of Science, Osaka University. He received a Doctor of Science degree in 2000 from Osaka University. He was a JSPS research fellow from 1997 to 2001. Since 2001, he has been a faculty member at Institute for Molecular Science. His research interests include near-field optics, plasmonics, and ultrafast phenomena in nanomaterials.

Hiromi Okamoto received B.S. (1983) and M.S. (1985) degrees from Department of Chemistry, Faculty of Science, The University of Tokyo. He received a Doctor of Science degree in 1991 from The University of Tokyo. He was appointed as a Research Associate at Institute for Molecular Science in 1985, where he developed femtosecond coherent Raman spectroscopic methods and studied vibrational dephasing in liquids. He then moved to The University of Tokyo in 1990, and was promoted to Associate Professor in 1993, where he studied vibrational relaxation phenomena using picosecond Raman spectroscopy, and also excited-state molecular structures/dynamics by using picosecond infrared spectroscopy in the fingerprint region. Since 2000, he has been serving as a Professor at Institute for Molecular Science. His present major research interests are near-field optical spectroscopic studies of nanomaterials, especially excited-state dynamics.